Mechanical, thermal and decomposition behavior of poly(epsilon-caprolactone) nanocomposites with clay-supported carbon nanotube hybrids

Terzopoulou, Zoe; Bikiaris, Dimitrios N.; Triantafyllidis, Konstantinos S.; Potsi, Georgia; Gournis, Dimitrios; Papageorgiou, George Z.; Rudolf, Petra

Published in:
Thermochimica Acta

DOI:
10.1016/j.tca.2016.09.001

Publication date:
2016

Thermochimica Acta 642 (2016) 67–80

Contents lists available at ScienceDirect

Thermochimica Acta

journal homepage: www.elsevier.com/locate/tca

Mechanical, thermal and decomposition behavior of poly(ε-caprolactone) nanocomposites with clay-supported carbon nanotube hybrids

Zoe Terzopoulou[a], Dimitrios N. Bikiaris[a,*], Konstantinos S. Triantafyllidis[a], Georgia Potsi[b,d], Dimitrios Gournis[b], George Z. Papageorgiou[c], Petra Rudolf[d]

[a] Department of Chemistry, Aristotle University of Thessaloniki, GR-54124 Thessaloniki, Greece
[b] Department of Materials Science and Engineering, University of Ioannina, GR-45110 Ioannina, Greece
[c] Chemistry Department, University of Ioannina, P.O. Box 1186, 45110 Ioannina, Greece
[d] Zernike Institute for Advanced Materials, University of Groningen, Nijenborgh 4, 9747 AG Groningen, The Netherlands, The Netherlands

ARTICLE INFO

Article history:
Received 21 July 2016
Received in revised form 1 September 2016
Accepted 2 September 2016
Available online 4 September 2016

Keywords:
Poly(ε-caprolactone)
Nanocomposites
Hybrid nanoparticles
Clay-supported carbon nanotubes
Thermal properties

ABSTRACT

Poly(ε-caprolactone) (PCL) nanocomposites with hybrid clay-supported carbon nanotubes (Clay-CNT) in concentrations 0.5, 1.0 and 2.5 wt% were prepared by melt mixing. Mechanical, structural and thermal properties of the nanocomposites were studied. All nanocomposites exhibited similar stress-strain patterns to those of neat PCL but, with increasing nanofiller content yield point and Young's Modulus values increased, despite the absence of chemical interactions between PCL and Clay-CNT. It was also found that the crystallinity of the nanocomposites is the same as for neat PCL, but the nanofiller acts as nucleating agent which promotes the crystallization and also allows it to occur at higher temperatures. Thermal stability is instead negatively influenced by the nanofiller, since Clay-CNT catalyzes the decomposition of PCL at lower temperature. The monomer ε-caprolactone is the main decomposition product resulting from intramolecular esterification while *cis*-elimination at ester bonds (β-hydrogen bond scission) is favored at higher temperatures.

1. Introduction

Poly(ε-caprolactone) (PCL) is an aliphatic polyester that can be produced either by the polycondensation of 6-hydroxyhexanoic acid or by ring-opening polymerization of ε-caprolactone. PCL is biodegradable, biocompatible, soluble in organic solvents, and allows easy thermal processing due to its low viscosity and melting point; it is commercially available [1]. PCL is used in a broad field of applications, including tissue engineering [2], drug delivery [3], microelectronics [4] and packaging [5]. Besides its attractive properties, PCL also has important disadvantages, like low melting temperature T_m, of ~60 °C, low modulus, low abrasion resistance, relative high cost and poor barrier properties.

Incorporation of nanofillers in polymeric matrices is a widely used technique for improving and controlling their properties. Nanoclays and carbon nanotubes (CNTs) are two of the most extensively studied nanofillers and have been shown to efficiently enhance mechanical, thermal and barrier properties of polymers [6,7]. How efficiently these nanofillers modify these properties directly depends on how well they are dispersed in the polymer matrix and for both clay platelets and CNTs the formation of agglomerates greatly reduces the beneficial effects of the nanoparticles. In this context, combining clays with carbon nanotubes is expected to further enhance the performance of polymers [8–10]. Addition of CNTs to PCL matrix results in poor mechanical and thermal properties because of lack of interactions and agglomeration of the nanofillers [11], but crystallization activity is enhanced in very small CNT contents [12]. Clay-CNT hybrids have indeed been used as nanofillers in polymers, with very promising results. Litina et al. found that the addition of Clay-CNTs to polystyrene-b-polyisoprene copolymer resulted in exfoliated structures with strong interfacial adhesion [13]. The same group prepared polystyrene-b-polyisoprene-b-polystyrene triblock copolymer with functionalized Clay-CNTs, which were well dispersed and exfoliated in the polymeric matrix and improved the mechanical properties [14]. Zhang et al. studied polyamide-6 nanocomposites with Clay-CNT hybrids, and discovered that the incorporation of just 1 wt% nanofiller resulted in an increase of tensile modulus and tensile strength by 290%

* Corresponding author.
E-mail address: dbic@chem.auth.gr (D.N. Bikiaris).

http://dx.doi.org/10.1016/j.tca.2016.09.001
0040-6031/

and 150%, respectively [15]. Epoxy nanocomposites with Clay-CNTs were found to possess an exfoliated structure and improved mechanical strength and hardness [16], while similar poly(vinyl alcohol) (PVA) nanocomposites exhibited improved thermal and dynamic mechanical properties [17]. Hybrid Clay-CNTs have also been added in other thermoplastics like poly(lactic acid) (PLA) and poly(ethylene terephthalate) (PET), and the nanocomposites produced had improved mechanical, barrier and thermal properties [18–20].

Although existing reports reveal that Clay-CNTs hybrids shows promising results as reinforcing additives, combining advantages of both layered clays and carbon nanotubes have not yet been studied with PCL. So, the aim of the present work is to synthesize novel Clay-CNTs hybrids and PCL/Clay-CNT nanocomposites with several nanofiller concentrations (0.5, 1 and 2.5 wt%), in order to evaluate the effect of nanofilles on structural, mechanical and thermal properties of PCL.

2. Experimental

2.1. Materials

PCL with molar mass Mn = 65,000 g/mol was purchased from Sigma-Aldrich. The clay used was a sodium-montmorillonite (Zenith-N) from Milos, Greece, with particle size ≈2 mm, obtained from Silver and Barytine Co. The structural formula for Zenith-N as determined from chemical analysis is: $Na_{0.92}$ $[Si_{7.75}$ $Al_{0.25}]\{Al_{3.21}Mg_{0.69}$ $Fe^{III}{}_{0.02}$ $Fe^{II}{}_{0.03}$ $Ti_{0.05}\}O_{20}(OH)_4$ [21] and its cation-exchange capacity (CEC) is 80.2 mequiv/100 g clay.

Clay-CNT hybrid nanoadditives were prepared as described previously [8,14]. Briefly, an amount of sodium clay (500 mg) was dispersed in water (100 mL) and reacted with 100 mL of an aqueous solution containing $NiCl_2{\cdot}6H_2O$ (0.01 M) and $FeCl_2{\cdot}6H_2O$ (0.01 M). The dispersion was stirred for 3 h, after which the Ni/Fe-exchanged clay was separated by centrifugation and rinsed repeatedly with distilled–deionized water. The material was then dried at room temperature and calcined at 450 °C for 4.5 h. Carbon nanotubes were synthesized by catalytic decomposition of acetylene over the Ni/Fe-clay catalyst in a fixed bed flow reactor at 700 °C [8]. About 100 mg of the catalyst was placed in an alumina boat, which was placed in a tubular furnace with an inner diameter of 2.2 cm and length of 90 cm. The catalyst was heated up to 700 °C under an argon (Ar) atmosphere and was then reacted with acetylene at the same temperature for 30 min using a feed flow of argon/acetylene mixture (10 and 90 cm^3/min, respectively). The catalyst was then cooled down to room temperature under pure argon and the formed clay–CNT hybrid material was collected from the ceramic boat.

2.2. PCL/Clay-CNT nanocomposites preparation

Nanocomposites containing 0.5, 1 and 2.5 wt% nanoadditives were prepared by melt mixing in a Haake-Buchler Reomixer (model 600) with roller blades and a mixing head with a volumetric capacity of 69 cm^3. Prior to melt-mixing the nanoadditives were dried by heating in a vacuum oven at 130 °C for 24 h. The two components were physically premixed before being fed in the reomixer, in order to achieve better dispersion of the nanoadditives in PCL. Melt blending was performed at 100 °C with 50 rpm for 5 min. During the mixing period the melt temperature and torque were continuously recorded. After preparation each PCL/Clay-CNT nanocomposite was milled and placed in a desiccator to prevent any moisture absorption.

2.3. Characterization

2.3.1. Mechanical properties

Measurements of the tensile mechanical properties of the prepared PCL/Clay-CNT nanocomposites were performed with the help of an Instron 3344 dynamometer, in accordance with ASTM D638, using a crosshead speed of 50 mm/min. Relatively thin sheets of about 350 ± 25 mm were prepared using an Otto Weber, Type PW 30 hydraulic press connected with an Omron E5AX Temperature Controller, at a temperature of 80 ± 5 °C. The moulds were rapidly cooled by immersing them in water at 20 °C. From these sheets, dumb-bell-shaped tensile test specimens (central portions 5 ± 0.5 mm thick, 22 mm gauge length) were cut in a Wallace cutting press and conditioned at 25 °C and 55–60% relative humidity for 48 h. From the stress-strain curves the values of Young's modulus, the elongation at break and the tensile strength were determined. At least five specimens were tested for each nanofiller concentration and the average values, together with their standard deviations, are reported.

2.3.2. Fourier-transform infrared spectroscopy (FTIR)

FTIR spectra of all the samples were obtained using a Perkin-Elmer FTIR spectrometer, model Spectrum One. The materials were in the form of thin films with thickness of approximately 30 μm. The IR spectra of these films in the spectral region of 400–4000 cm^{-1} were obtained collecting 64 scans in the absorbance mode with a resolution of 4 cm^{-1}.

2.3.3. X-Ray diffraction (XRD)

XRD studies of all the samples, in the form of films, were performed using a MiniFlex II XRD (Rigaku) system over the 2θ range between 5 and 60°, with steps of 0.05° and a counting time of 5 s. Crystallinity calculations of the studied materials were performed by fitting the WAXD profiles with Gaussian-Lorentzian cross product curves and deriving the ratio of crystalline over overall fitted peaks area.

2.3.4. Raman spectroscopy

Raman spectra in the range of 200–3500 cm^{-1} were recorded with a Micro-Raman system RM 1000 Renishaw using a laser excitation line at 532 nm (Nd–YAG). A power of 1 mW was used with 1 μm focusing spot in order to avoid photodecomposition of the samples.

2.3.5. X-ray photoelectron spectroscopy (XPS)

For the XPS measurements, samples were introduced via a load-lock system into a SSX-100 (Surface Science Instruments) photoelectron spectrometer with a monochromatic Al Kα X-ray source ($h\nu$ = 1486.6 eV). The base pressure in the spectrometer was 1×10^{-9} Torr during measurements. The energy resolution was set to 1.21 eV. The photoelectron takes off angle was 37° with respect to the surface normal. An electron flood gun providing 0.2 eV kinetic energy electrons in combination with a gold grid mounted about 1 mm above the sample was used to compensate for sample charging. A second round of measurements was performed without the gold grid in order to compare to data in the literature [22]. All binding energies were referenced to the C1s core level of the C—C bond, set to the nominal value of 285.0 eV [23].

2.3.6. Thermogravimetry (TG)

Thermogravimetric analysis was carried out with a Setsys 16/18 TG-DTA (Setaram). Samples (4 ± 0.2 mg) were placed in alumina crucibles and heated from ambient temperature to 600 °C at 20 °C/min in a 50 mL/min flow of N_2; an empty alumina crucible was used as reference.

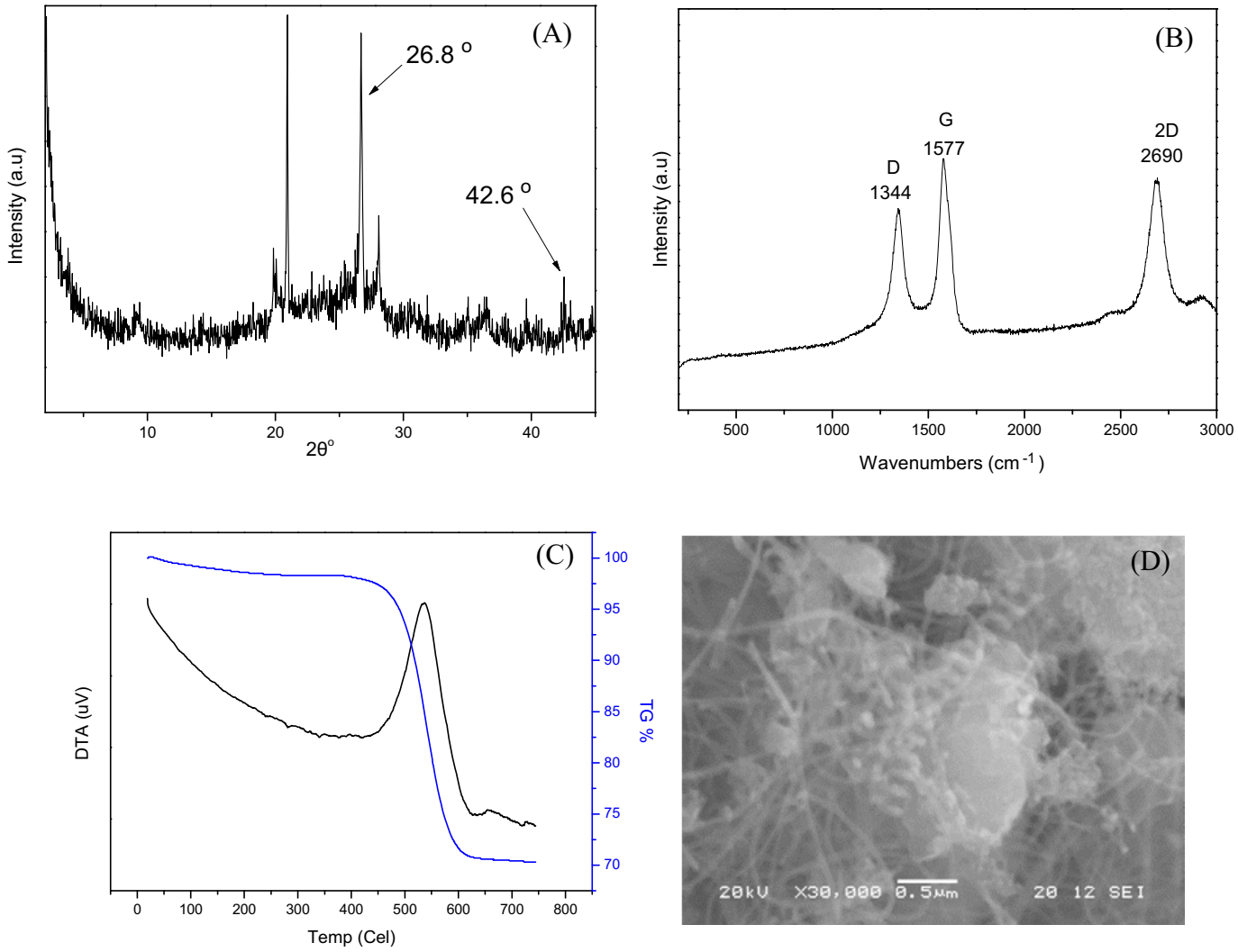

Fig. 1. X-Ray diffraction pattern (A), Raman spectrum (B), DTA/TGA diagrams (C) and SEM micrograph (D) of the Clay-CNT hybrid produced by catalytic decomposition of acetylene over the Ni/Fe-clay catalyst in a fixed bed flow reactor at 700 °C.

2.3.7. Pyrolysis-gas chromatography–mass spectroscopy (Py-GC/MS)

For Pyrolysis-gas chromatography/mass spectroscopy (Py-GC/MS) analysis of PCL and PCL/Clay-CNT nanocomposites, a very small amount of each sample (6 mg) was placed initially into the sample cup of a Multi-Shot EGA/PY-3030D Pyrolyzer (Frontier Laboratories Ltd, Fukushima, Japan) and from there fell free into the Pyrolyzer furnace. The pre-selected pyrolysis temperatures were 370 and 400 °C and the GC oven temperature was programmed from 50 to 300 °C at 20 °C/min. The sample vapors generated in the furnace were split (at a ratio of 1/50), a portion moved to the column at a flow rate of 1 mL/min and the remaining portion exited the system via the vent. The pyrolyzates were separated in the Ultra Alloy metal capillary column (UA$^+$5) and analyzed by the MS detector GC–MS-QP2010 Ultra (Shimadzu, Japan).

2.3.8. Differential scanning calorimetry (DSC)

A Perkin–Elmer, Pyris Diamond DSC differential scanning calorimeter, calibrated with pure Indium and Zinc standards, was used. The system also included an Intracooler 2P cooling accessory, in order the DSC apparatus to achieve function at sub-ambient temperatures and high cooling rates. Samples of 5 ± 0.1 mg, sealed in aluminium pans, were used to test the thermal behavior of the nanocomposites. In case of isothermal crystallization tests, the samples were heated at a rate 20 °C/min to 90 °C, kept at that temperature for 3 min to erase the previous thermal history and cooled to the crystallization temperature at a rate 100 °C/min. After complete crystallization the samples were heated at 20 °C/min to 90 °C. In case of non-isothermal crystallization experiments the samples were heated at 20 °C/min to 90 °C, kept at that temperature for 3 min and then cooled to 0 °C at different cooling rates. The tested cooling rates were 2.5, 5, 7.5, 10, 15 and 20 °C/min.

2.3.9. Polarized light optical microscopy (PLOM)

A polarizing light microscope (Nikon, Optiphot-2) equipped with a Linkam THMS 600 heating stage, a Linkam TP 91 control unit and a Jenoptic ProgRes C10Plus camera was used for PLM observations.

2.3.10. Scanning electron microscopy (SEM)

Scanning electron images were recorded using a JEOL JSM–5600 V scanning electron microscope. The samples were coated with a thin film of conducting metal (Au) to avoid charging problems. All images shown are typical and representative of the samples under observation.

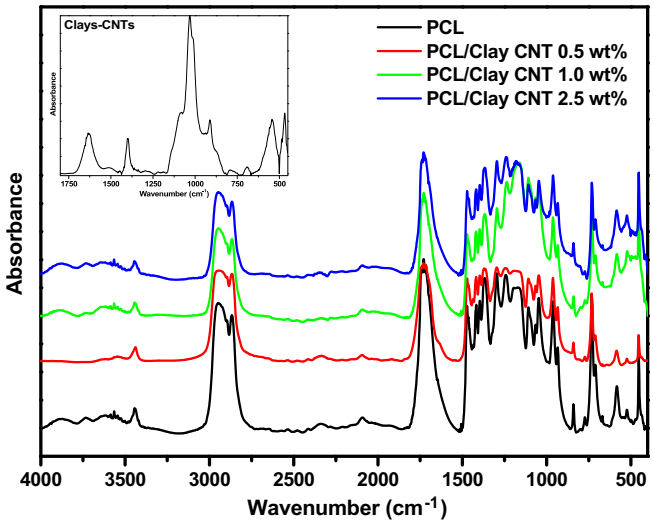

Fig. 2. FTIR spectra of PCL and PCL/Clay-CNT nanocomposites. Inset: FTIR spectrum of pristine Clay-CNT.

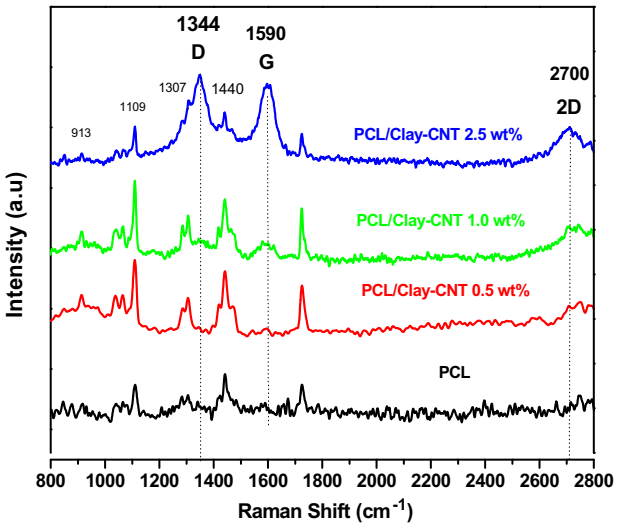

Fig. 3. Raman spectra of PCL and PCL/Clay-CNT nanocomposites with different amounts of filler.

3. Results and discussion

3.1. Characterization of the clay-CNT hybrid

For the synthesis of the Clay-CNT hybrid, montmorillonite clay was loaded with nickel and iron cations that function as catalysts in the growth of carbon nanotubes via catalytic decomposition of acetylene. This bimetallic system was chosen because it results in higher yields of synthesized CNTs since the synergistic action of the two metals enhances the total catalytic activity [24,25]. The XRD pattern of the Clay-CNT hybrid, presented in Fig. 1A, shows a weak peak in the lower 2θ range with a maximum at 9.25°; this 2θ value corresponds to a d_{001}-spacing of 9.6 Å, which equals the thickness of the layer of 2:1 clay minerals in the absence of water. The intensity of the 001 peak is quite low, implying that after the production of CNTs on the surface of the clay layers, the majority of the latter has lost their ordered stacking and exhibits an exfoliated structure. In the same pattern, peaks at 2θ = 26.8° and 42.6°, corresponding to the 002 and 100 reflections of graphite, are also present, revealing the successful production of good quality multiwalled CNTs [26,27].

The Raman spectrum of the Clay-CNT hybrid, shown in Fig. 1(B), exhibits a very intense peak at 1577 cm^{-1} (G-Band) corresponding to the tangential stretching (E2g) mode of highly oriented pyrolytic graphite (HOPG), and a weaker band near 1344 cm^{-1} (D-Band), which originates from disorder in the sp^2-hybridized carbon atoms, characteristic of lattice distortions in the curved graphene sheets and/or tube ends. In addition, the 2D band, which is a second-order two-phonon mode, is also present in the spectrum [28]. The relative intensity of D with respect to the G-band (I_D/I_G) reveals the degree of disorder in the graphite sheets, and is therefore indicative of the quality of the synthesized CNTs [24,25,29]. More specifically, the I_D/I_G ratio for the Clay–CNT hybrid was calculated as 0.73, a value which is lower than reported in the literature (I_D/I_G = 0.85–1.3) for CNTs prepared using acetylene as a carbon source [9,30–33].

The high quality of the produced CNTs was further confirmed by thermogravimetric analysis (DTA/TGA), which also allows to determine the percentage of deposited carbon (and hence the percentage of CNTs). The DTA/TGA curves of the Clay-CNT hybrids are presented in Fig. 1(C). The DTA curve shows an intense endothermic peak at 540 °C, which is assigned to the oxidation (destruction) of the nanotubes; this high temperature indicates that the CNTs are pure and present few defects [34]. From the weight loss in the TGA curve one can calculate that the carbon nanotubes correspond to about 30 wt% of the total mass.

The representative SEM micrograph of the Clay-CNT hybrid in Fig. 1(D) reveals an abundance of multiwalled carbon nanotubes with an average diameter between 20 and 35 nm and lengths up to several micrometers. The successful creation of a three-dimensional network of carbon nanotubes and aluminosilicate nanoplatelets is evident from the fact that the CNTs are rooted on the clay layers and the clay platelets are clearly in a delaminated state.

3.2. Characterization of the composition and structure of the nanocomposites

The nanocomposites were studied by FTIR, Raman and XPS spectroscopies in order to confirm the presence of the hybrid nanoadditive in the polymer mass and to evaluate possible interactions between PCL and nanofillers [35].

FTIR spectra of pure PCL, Clay-CNTs and their nanocomposites are shown in Fig. 2. The main peaks of PCL are clearly distinguished; CH_2 stretching is responsible for peaks at 2945 and 2865 cm^{-1}, carbonyl and C—O stretching appear at 1730 cm^{-1} and 1240 cm^{-1} respectively. For Clay-CNT absorption bands are present at 1630 cm^{-1} (C=C stretching), 1400 cm^{-1} (aromatic C—C stretching), 1090 cm^{-1} (C—O stretching), 1030 cm^{-1} (Si—O—Si), 912 cm^{-1} (—OH bending), 543 cm^{-1} (Si—O—Si) and 469 cm^{-1} (Si—O). As can be seen clays have some surface silanol groups that could interact with PCL. However, from Fig. 2 it is clear that in all nanocomposites the characteristic peaks of PCL are recorded at the same positions as in the pure compound; in particular no shift is detected for the band of the carbonyl groups. However, this band at 1730 cm^{-1} is very broad and with such low Clay-CNT contents an additional feature from interacting moieties might be impossible to detect.

Raman spectra of PCL and its nanocomposites are presented in Fig. 3. In spectrum of pure PCL, the peak at 1440 cm^{-1} is assigned to the methylene groups (CH_2) of the crystalline phase of PCL, while peaks detected at 1109 cm^{-1} and 913 cm^{-1} stem from C—O—C and C—COO vibrations of PCL [36]. Comparing the spectrum of neat PCL with those of the reinforced PCL/Clay-CNT samples, one recognizes the contribution of the carbon nanotubes in all the spectra of the nanocomposites. More specifically, for PCL/Clay-CNT with 2.5 wt% of nanofiller two more peaks are clearly observed at 1344 and 1590 cm^{-1} which can be assigned to the graphite D- and G-bands,

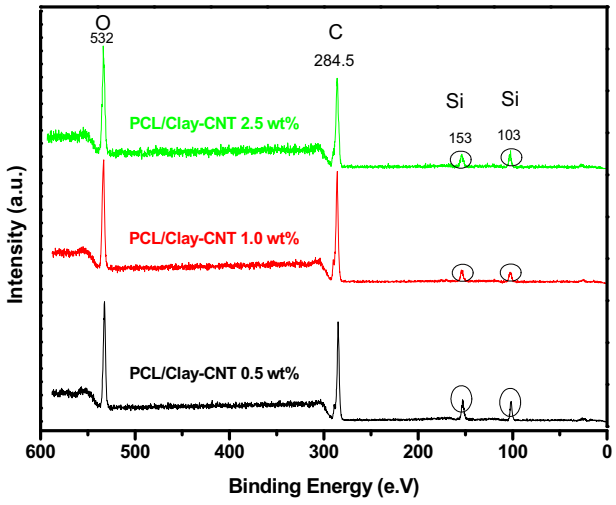

Fig. 4. XPS spectra of PCL and PCL/Clay-CNT nanocomposites with different amounts of filler.

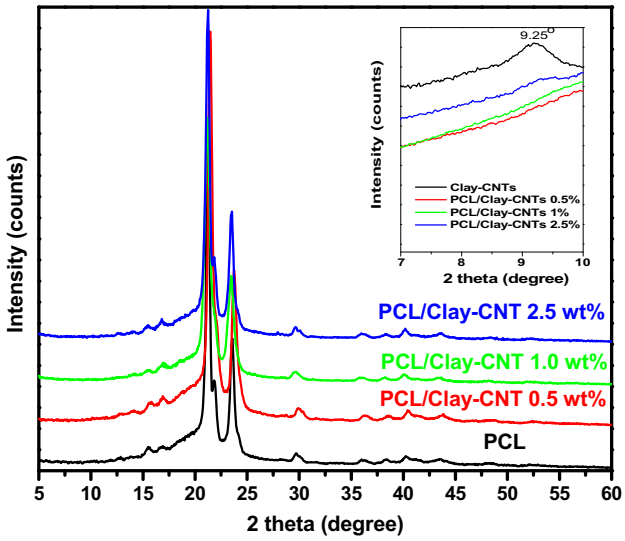

Fig. 5. X-Ray diffraction patterns of PCL, Clay-CNT and PCL/Clay-CNT nanocomposites. Inset: Detail of the same patterns at low angles.

respectively, and testify to the presence of the CNTs in the polymer matrix [37]. In addition, the 2D band peak at approximately 2700 cm^{-1} that is characteristic of sp^2 carbon with defects leading to sp^3 carbon atoms [38] is also present.

XPS spectroscopy was also employed to verify the presence of the Clay-CNT nanofiller in the PCL matrix. Fig. 4 presents the XPS survey spectra of all PCL/Clay-CNT nanocomposites. As labeled in spectra, characteristic photoelectron and Auger peaks of O, Si, and C are clearly distinguishable for all nanocomposite samples. In fact, the presence of the two silicon core level lines at 103 eV (Si2*p*) and 153 eV (Si2*s*) reveals the presence of the aluminosilicate mineral in the PCL composites. However, the dispersion of the filler in the polymer matrix was non-uniform, as can be seen in Fig. 4 from the fact that the Si core level photoemission intensity is not proportional to the nominal loading with Clay-CNT; for a composite with a certain composition we recorded spectra with different Si core level intensities (not shown). Hence it was not possible to quantify the amount of Si in the samples.

Another important factor which influences the final mechanical properties of nanocomposites is crystallinity [39]. Therefore, crystallinity was studied with X-Ray diffraction and differential scanning calorimetry (DSC); the latter will be discussed in Section 3.4. Diffraction patterns of Clay-CNT, neat PCL and their nanocomposites are presented in Fig. 5. In all nanocomposites the characteristic peaks of PCL at $2\theta = 21.25^\circ$ and 23.58°, attributed to the [110] and [200] crystallographic planes of the PCL crystal, respectively [40] were recorded; this indicates that the crystal structure of PCL is not altered by the addition of the hybrid nanoadditive. Moreover, the absence of the 001 diffraction peak at $2\theta \approx 9.3^\circ$ (due to ordered stacking of clay layers) in the patterns of all the final nanocomposites (Fig. 5 inset) suggests exfoliated structures, where all the individual clay platelets have been effectively dispersed within the polymeric mass. However, due to the small amount of nanofillers might be insufficient to render significant reflections.

Table 1
Crystallinity% of the nanocomposites as calculated by X-Ray diffraction patterns.

Sample	X (%)
PCL	40.08
PCL/Clay-CNT 0.5 wt%	46.58
PCL/Clay-CNT 1.0 wt%	50.32
PCL/Clay-CNT 2.5 wt%	53.75

The values of crystallinity% calculated by X-Ray diffraction patterns are presented in Table 1.

3.3. Mechanical properties of PCL/Clay-CNT nanocomposites

The mechanical properties of PCL and of the prepared PCL/Clay-CNT nanocomposites were calculated from stress-strain curves (presented in the Supporting information) and are summarized in Table 2. Stress-strain curves of PCL initiated with a steep linear increase, due to elastic deformation, followed by a yield point. Plastic deformation, which consists of orientation of the macromolecular chains in the direction of the applied force, occurred next, followed by stress hardening and finally breaking of the specimens. All nanocomposites exhibited similar stress-strain patterns. Increasing the nanofiller content resulted in a higher yield point and higher Young's Modulus values. Elongation was increased only at 0.5 wt% filler content, while tensile strength was slightly improved as compared to neat PCL for filler concentrations 0.5 and 1 wt%. The effect of the filler content on tensile strength and elongation at break are presented in Table 2. It is obvious that the optimum Clay-CNT concentration with regards to tensile strength and elongation at break is 0.5 wt%, since beyond that critical concentration those values begin to decrease. It is possible that this decrease is due to agglomeration and lack of interfacial bonding between PCL and Clay-CNT. However, stiffness is significantly increased, with

Table 2
Mechanical properties of PCL and PCL/Clay-CNT nanocomposites.

Sample	Tensile strength at break point (MPa)	Tensile strength at Yield point (MPa)	Strain at break (%)	Young's Modulus (MPa)
PCL	19.31 ± 0.35	14.33 ± 0.33	474.22 ± 14.62	181.15 ± 16.20
PCL/Clay-CNT 0.5 wt%	20.36 ± 1.67	15.05 ± 1.07	513.23 ± 36.33	195.17 ± 34.17
PCL/Clay-CNT 1.0 wt%	20.02 ± 0.54	16.02 ± 0.90	439.62 ± 40.26	218.95 ± 21.50
PCL/Clay-CNT 2.5 wt%	16.24 ± 2.38	17.68 ± 2.40	282.98 ± 39.03	332.49 ± 53.24

Young's modulus values up by 83% with 2.5 wt% filler, compared to neat PCL. The increased Young's modulus is caused by the enhanced crystallinity of the nanocomposites. It was reported that the incorporation of just 1.0 wt% Clay-CNT in polyamide-6 lead to high increase of tensile strength (from 18.5 to 46.8 MPa), while elongation decreased as expected [15]. This behavior was attributed to the good dispersion observed in TEM images; it is also possible that the secondary amino groups of polyamide strongly interact with the hydroxyls of the fillers. However, such strong enhancement on the mechanical properties is not observed in our PCL/Clay-CNT nanocomposites, maybe due to the absence of interactions between the reactive groups of PCL and of the hydrid nanofillers.

3.4. Isothermal and non-isothermal crystallization study of nanocomposites

The melting of PCL and of PCL/Clay-CNT samples crystallized at given crystallization temperatures was followed by differential scanning calorimetry. As shown in Fig. 6a the melting temperature (maximum of the DSC trace) shifted to slightly higher values when the sample was crystallized at higher temperature. This shows that the stability of the crystals increases with increasing crystallization temperature. The isothermal crystallization from the melt of neat PCL and of the nanocomposites was studied by DSC and PLOM. The rate of crystallization decreased drastically with increasing the temperature. However, in contrast to what was observed for the neat PCL, the phenomenon was still relatively fast even at 50 °C for the nanocomposites. Crystallization is complex phenomenon, involving nucleation and crystal growth. The presence of the nanofiller induces heterogeneous nucleation, so the overall rate of crystallization is faster in the composites even at high temperatures close to the melting temperature.

Assuming that the crystallinity increases linearly with the heat released during the crystallization, the relative degree of crystallinity, $X(t)$, can be obtained from isothermal experiments according to the following equation [41]:

$$X(t) = \frac{\int_0^t (dH_c/dt)dt}{\int_0^\infty (dH_c/dt)dt} \quad (1)$$

where dH_c denotes the measured enthalpy of crystallization during an infinitesimal time interval dt.

The crystallization half-time is defined as the time needed for the sample to achieve half of the maximum achievable crystallinity at a given temperature. From the plots of the relative degree of crystallinity with time, the crystallization half-time values for the materials studied in this work were determined. A decrease in the crystallization half-times for given crystallization temperature was found for the nanocomposites which shows that isothermal crystallization proceeds faster. The inverse of the crystallization half-time can be used as a measure of the overall crystallization rate. The plots of the overall crystallization rate with temperature presented in Fig. 6b show that at a given temperature the crystallization rate scales with the nanofiller content in the composites. Furthermore, in contrast to neat PCL, crystallization of the composites is fast even at high temperatures and needs relatively short times. For example, crystallization was performed at a temperature as high as 55 °C for the composites with 1 or 2.5 wt% filler content (Fig. 6c). Also, it is clear that in all studied temperatures crystallization rate increases by increasing the Clay-CNTs content. This phenomenon is attributed to the heterogeneous nucleation caused by the filler particles.

Polarized Light Optical Microscopy (PLOM) was used to follow the morphological evolution during isothermal crystallization from the melt. Typical observations are presented in Fig. 7, which illustrates that the addition of the nanofiller in the polymeric matrix

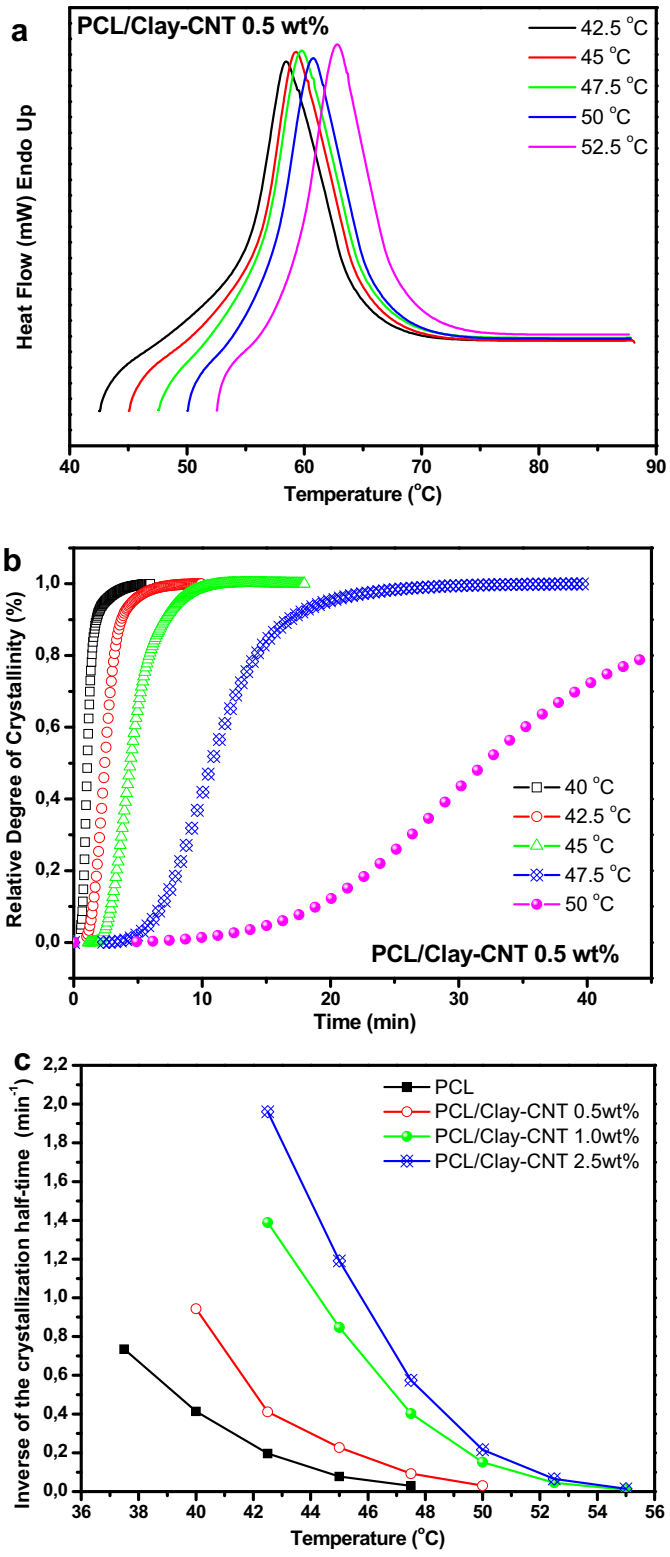

Fig. 6. a) Melting of PCL/Clay-CNT 1 wt% crystallized at different temperatures, b) relative degree of crystallinity vs time for PCL/Clay-CNT 0.5 wt% and c) crystallization rate as a function of crystallization temperature for neat PCL and PCL/Clay-CNT nanocomposites.

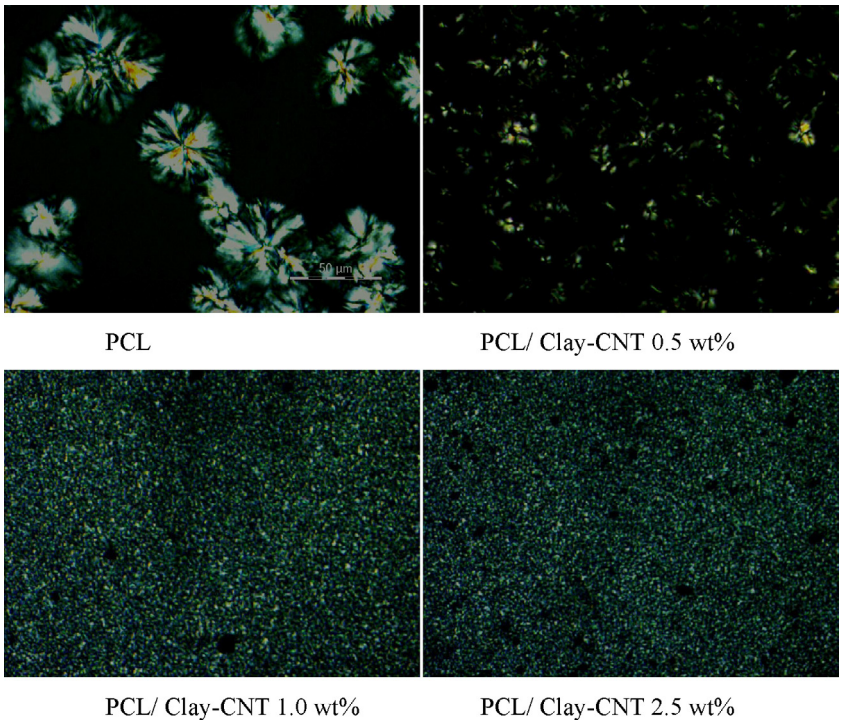

Fig. 7. Spherulites grown at 47.5 °C for neat PCL (a), PCL/Clay-CNT with 0.5 wt% (b), PCL/Clay-CNT with 1 wt% (c) and PCL/Clay-CNT with 2.5 wt% nanofiller(d).

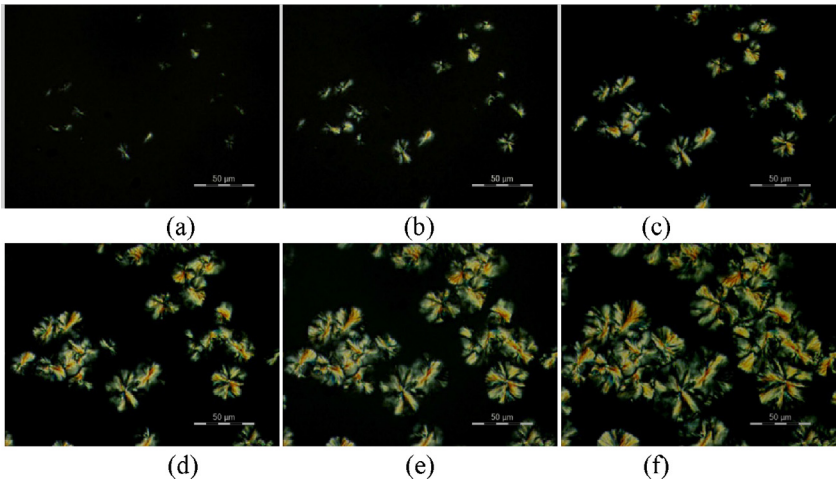

Fig. 8. Spherulites grown at 45 °C for neat PCL a) 30 s, b) 60 s, c) 120 s, d) 180 s, e) 240 s and f) 360 s.

leads to a spectacular increase in the nucleation rates accompanied by a strong decrease of the spherulites' size. Fig. 7a shows the spherulites of neat PCL at 47.5 °C; a significant increase in the number of spherulites can be seen in Fig. 7b–d for PCL/Clay-CNT with an increasing nanofiller content, namely 0.5 wt%, 1 wt% and 2.5 wt%. This is a clear proof that the Clay-CNT hybrids can act as nucleating agent which promotes the crystallization of PCL.

The Avrami equation is usually used to describe the space-filling effect of growing spherulites during isothermal crystallization process [41]:

$$\phi(t) = 1 - \exp[-\frac{3}{4}\pi N G^3 (t - t_o)^3] \quad (2)$$

where $\Phi(t)$ is the degree of space filling, N is the nucleation density, and $G(t)$ is the spherulitic growth rate.

The nucleation density, N, can be estimated from the degree of space-filling, $\Phi(t)$, using the Avrami equation:

$$N = \frac{-3\ln[1 - \phi(t)]}{4\pi G(t)^3 (t - t_o)^3} \quad (3)$$

The degree of space-filling $\Phi(t)$ can be considered as the relative degree of crystallinity. The spherulitic growth rate was assumed to be constant for PCL and the nanocomposites at given temperature, as significant interactions did not take place between the polymer and the filler. So, the spherulitic growth rate $G(t)$ was calculated from the PLOM data for the variation of the spherulite radius with time during crystallization of neat PCL at 45 and 47.5 °C. Figs. 8 and 9 show the growth of the sperulites for PCL with at 45 and 47.5 °C respectively, while Fig. 10 shows the plots of the spherulite radius with time prior to calculate $G(t)$.

The calculated nucleation density (N) values of the nanocomposites differ significantly with that of PCL (Fig. 11). N increases with

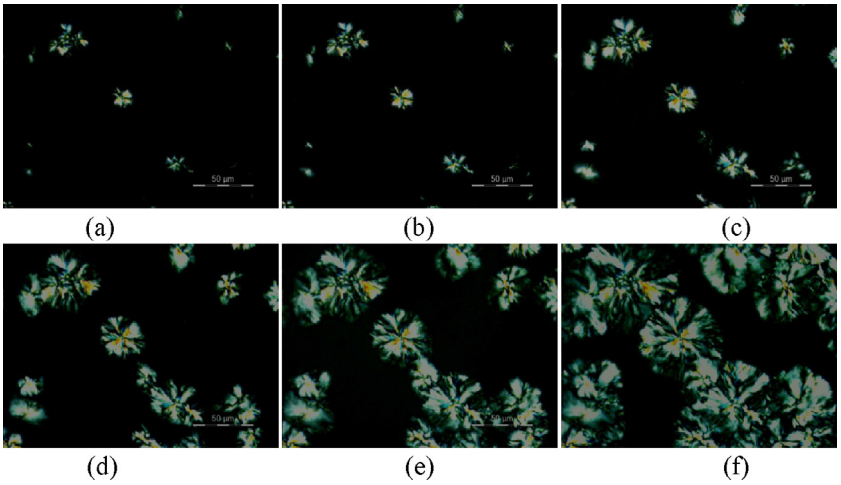

Fig. 9. Spheroulites grown at 47.5 °C for neat PCL a) 60 s, b) 120 s, c) 240 s, d) 300 s, e) 600 s and f) 960 s.

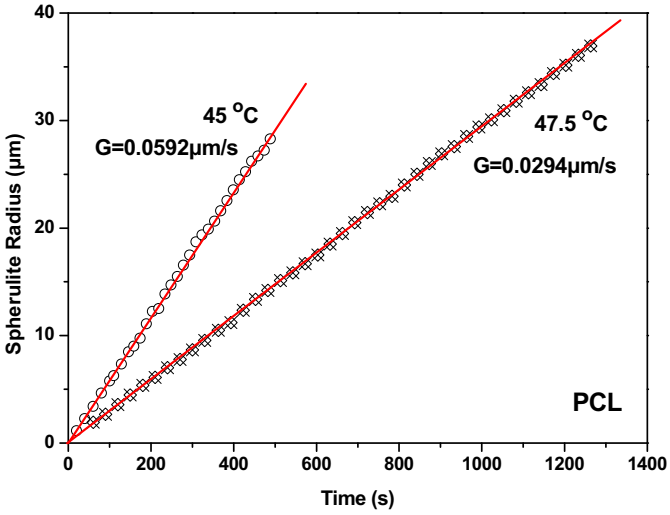

Fig. 10. Plots of the spherulite radius vs time for neat PCL at 45 and 47.5 °C.

the filler content. However, in case of the higher content (2.5 wt%) the nucleation activity seems to be lower than expected. Fig. 11b shows that the nucleation density of the nanofiller does not change with temperature. The fact that the nuclei number is constant indicates the heterogeneous nature of the process. In contrast, for neat PCL the nucleation density at 47.5 °C is about half that at 47.5 °C (Fig. 11d). Obviously these findings prove the different nucleation mechanism.

Non-isothermal crystallization of the nanocomposites was also studied using DSC, always in comparison to that of neat PCL. With increasing the cooling rate, the peak appeared at steadily lower temperature and a peak broadening was observed. With increasing filler content, a clear shift of the crystallization peak towards the high temperatures was observed, due to the faster crystallization (Fig. 12a). Finally, further increase of the filler content above 1.0 wt% has only a limited effect.

The crystallization temperature T_c, can be converted to crystallization time, t, with the well-known relationship for non-isothermal crystallization processes that is strictly valid when the sample experiences the same thermal history as designed by the DSC furnace [41]:

$$t = \frac{(T_o - T_c)}{\beta} \tag{4}$$

where β is the constant cooling rate, T_o is the temperature at the beginning of crystallization and T_c is the crystallization temperature at time t. So, the experimental data for degree of crystallinity as function of temperature obtained from the DSC cooling scans were transformed to data as a function of time. The time of crystallization was shorter when cooling at fast rates. However, for given cooling rate, the crystallization time decreased with increasing filler content.

To evaluate the nucleation activity of the filler in the non-isothermal crystallization, we applied the method of Gatzow and Dobreva for the nucleation activity of foreign substrates in polymer melt using DSC data from non-isothermal crystallization, [42,43] this method has also been used in previous works for nanocomposites [44,45].

The nucleation activity, φ, is the factor by which the work of three-dimensional nucleation decreases when a foreign substrate is added. If the foreign substrate is extremely active, the nucleation activity tends to 0; if the foreign substrate is inert, φ is close 1. The nucleation activity is calculated from the ratio:

$$\phi = \frac{B^*}{B} \tag{5}$$

where B is a parameter that can be calculated from the following equation

$$B = \frac{\omega\sigma^3 V_m^2}{3nk_B T_m^0 \Delta S_m^2} \tag{6}$$

where ω is a geometric factor, σ is specific free energy, V_m is the molar volume of the crystallizing substance, n is the Avrami exponent, ΔS_m is the entropy of melting and $T_m{}^0$ the equilibrium melting temperature which was assumed to be 74 °C for PCL [46].

Furthermore, B can be experimentally determined from the slope of Eq. (7) obtained by plotting ln(β) versus the inverse squared degree of supercooling $1/\Delta T_p{}^2$ where $\Delta T_p = T_m - T_p$ [43]

$$\ln\beta = Const - \frac{B}{\Delta T_p^2} \tag{7}$$

The above equation holds for homogeneous nucleation from a melt, near the melting temperature. By using a nucleating agent, Eq. (3) is transformed to the following equation for heterogeneous nucleation:

$$\ln\beta = Const - \frac{B^*}{\Delta T_p^2} \tag{8}$$

Fig. 12b shows the plots of ln(β) versus $1/\Delta T_p{}^2$ for neat PCL and for the PCL/Clay-CNT nanocomposites. As it can be seen, straight

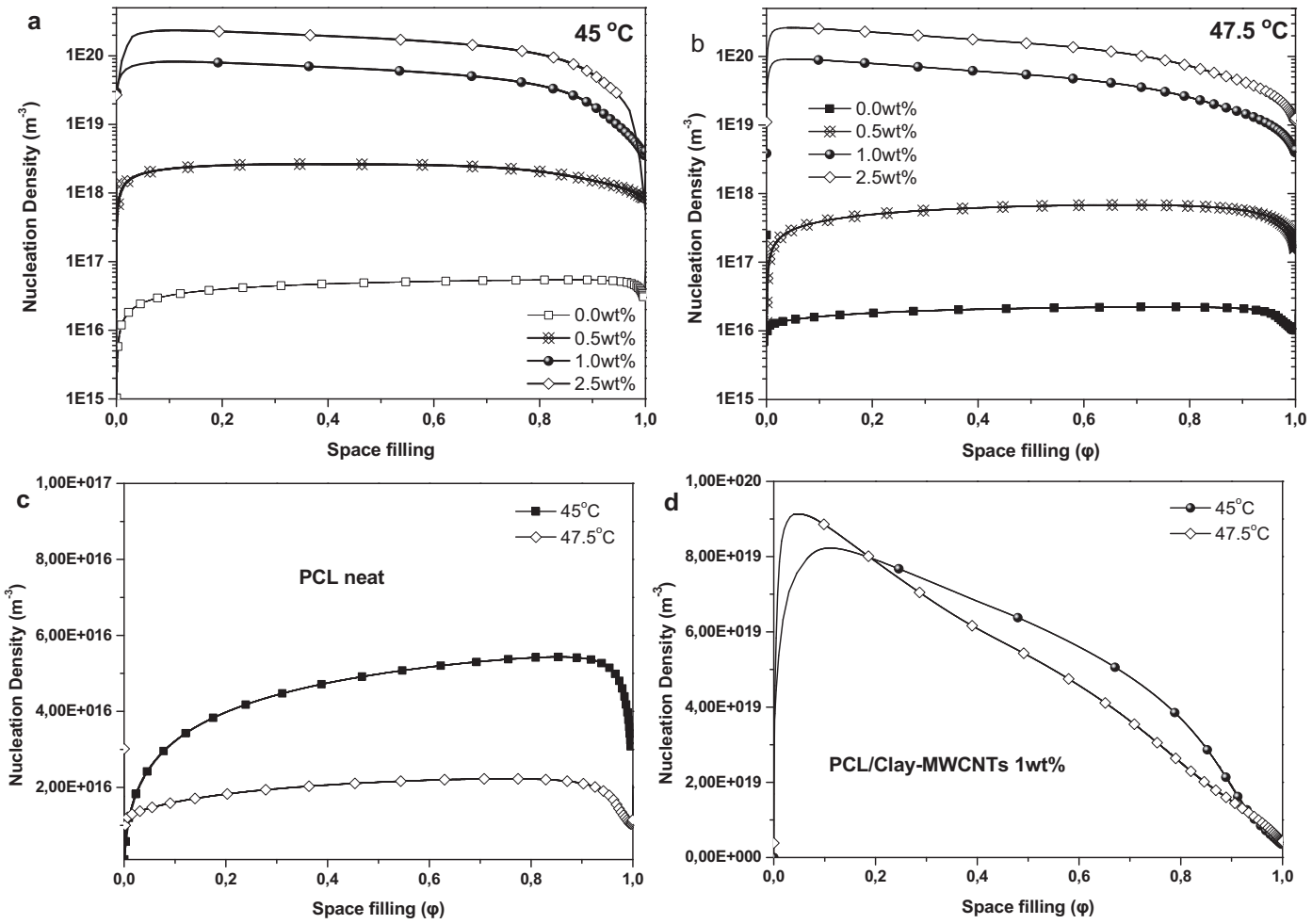

Fig. 11. Nucleation density for: a) and b) PCl and the nanocomposites at 45 and 47.5 °C respectively, c) neat PCL at 45 and 47.5 °C and d) PCL/Clay-MWCNTs 1 wt% at 45 and 47.5 °C.

lines are obtained in every sample. The values of B and B^* for the plain PCL and the PCL/Clay-CNT nanocomposites respectively, were calculated from the slopes of the lines. Then, the nucleation activity was computed from Eq. (3) and presented in Fig. 12c. It is important to refer at this point that a value of φ close to zero indicates high nucleation activity, while values close to 1 show low activity. The plot in Fig. 12c shows the variation of the nucleation activity of the Clay-CNT filler with the filler content in the PCL/Clay-CNT nanocomposites. As can be seen a value of 0.53 was reached in case of 1.0 wt% content. Further increase in the filler content, led to a slight decrease, reaching φ = 0.48. It seems that a plateau was reached.

3.5. Thermal stability and decomposition mechanism of nanocomposites

TGA thermograms of PCL and of the PCL/Clay-CNT nanocomposites are presented in Fig. 13. Thermal degradation occurs in one step for all samples and starts at 350 °C. Table 3 shows the values of the temperature at which degradation occurs with the highest rate, T_p, and temperatures where 5 wt% and 50 wt% mass losses have occurred respectively, $T_{d,5\%wt}$ and $T_{d,50\%wt}$. After degradation the solid residue at 600 °C, also reported in the table, increased from 0.09 wt% for neat PCL to 2.47 wt% for PCL/Clay-CNT with 2.5 wt% filler, which is very close to the added filler amount, due to the non-degradable inorganic clays and graphitic content of the nanofillers.

Table 3
TGA results for PCL and PCL/Clay-CNT nanocomposites.

Sample	T_p (°C)	$T_{d,5\%wt}$ (°C)	$T_{d,50\%wt}$ (°C)	Residue at 600 °C (wt%)
PCL neat	429.3	390.7	427.0	0.09
PCL/Clay-CNT 0.5 wt%	428.4	389.0	427.2	1.02
PCL/Clay-CNT 1.0 wt%	427.0	380.4	425.4	1.53
PCL/Clay-CNT 2.5 wt%	429.5	374.4	427.2	2.47

As can be seen from the recorded thermograms, PCL and its nanocomposites exhibited relatively good thermal stability, with no significant mass loss up to 300 °C. All the characteristic TGA temperatures are similar for all samples, with a slight decreasing trend for filler concentrations up to 1.0 wt%, and a slight, almost negligible increase for the 2.5 wt% sample. While Clay-CNT in concentrations 1–7 wt% has been found to increase thermal stability of PET and PVA [17,20], the opposite effect has been observed for PLA [19]. It is noteworthy that Clay-CNT used as fillers in the studies concerning PET and PVA were subjected to a strong acid treatment for metal catalyst removal and this treatment can also oxidize hydroxyl groups of CNTs to carboxyls. In the case of PLA, no such treatment was performed. The negative effect of the nanofillers on thermal stability of PLA was therefore explained by the presence of iron oxide residues from the Clay-CNT synthesis that can promote breaking of the polymer's macromolecular chain. This could be true in our study too. Clay-CNT would be expected to act as mass transport barriers to volatile degradation products, therefore increasing thermal

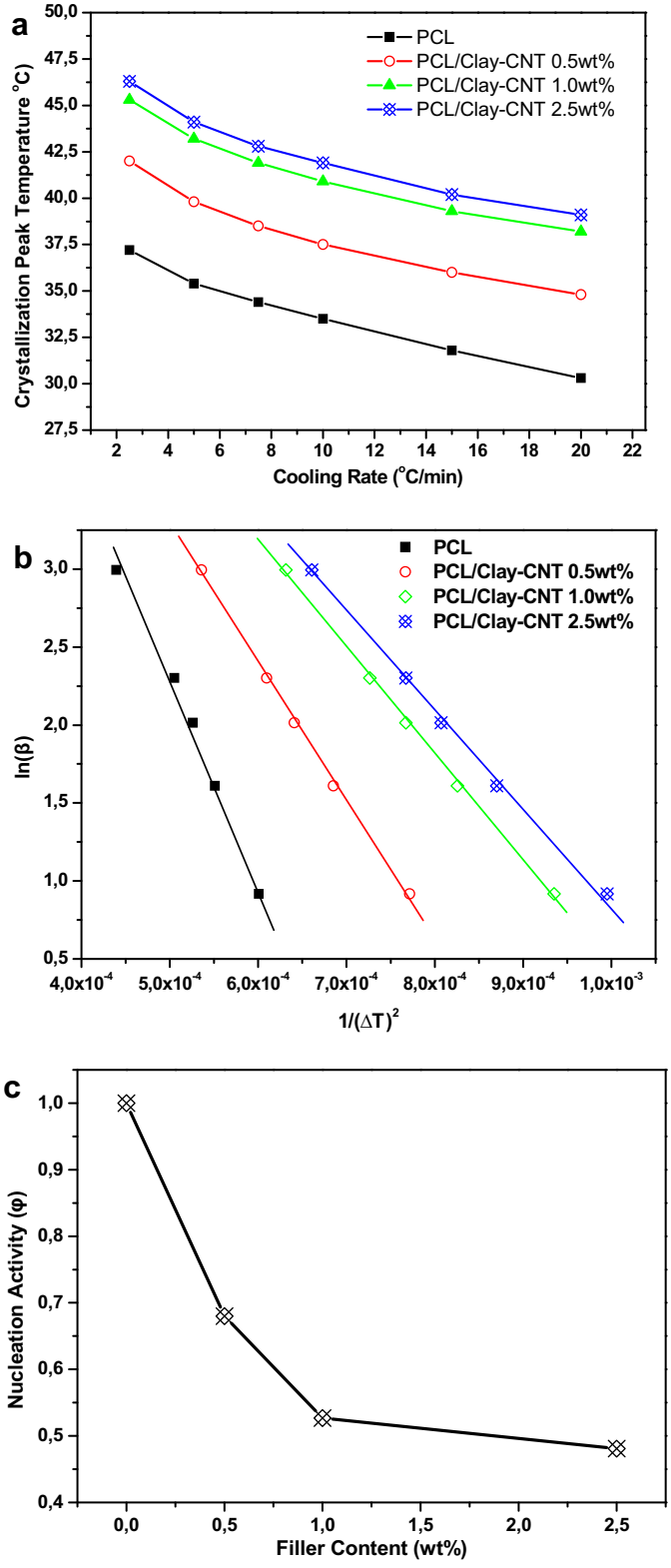

Fig. 12. (a) Crystallization temperature vs cooling rate, (b) plots of ln(β) versus $1/\Delta T_p^2$ and (c) nucleation activity of the Clay-CNT filler as a function of filler content in the PCL/Clay-CNT nanocomposites.

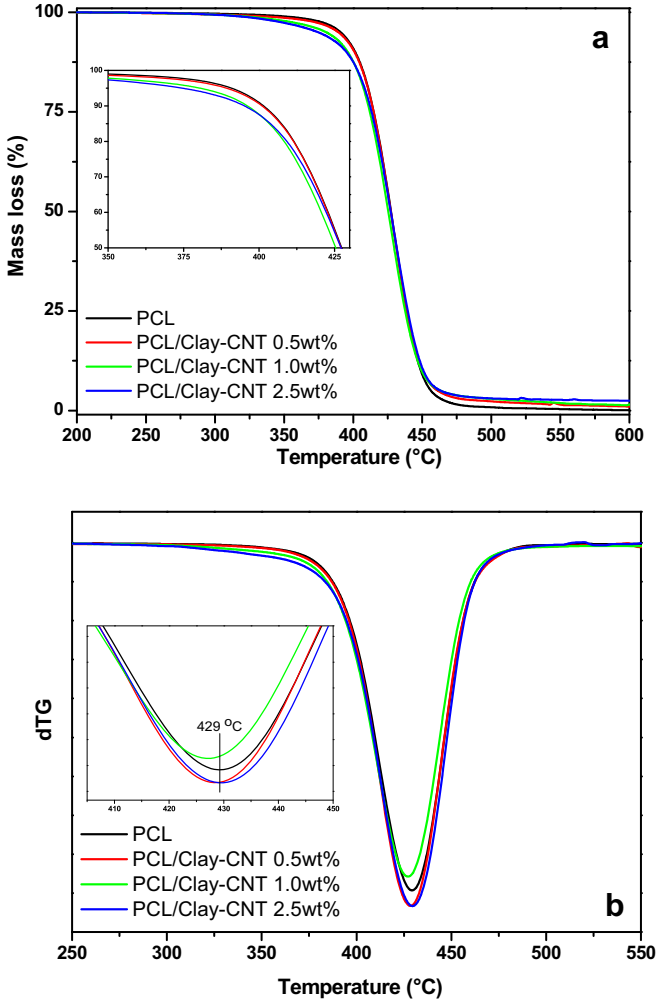

Fig. 13. (a) Mass loss curves and (b) derivative of the mass loss curves (DTG) for neat PCL and PCL/Clay-CNT nanocomposites.

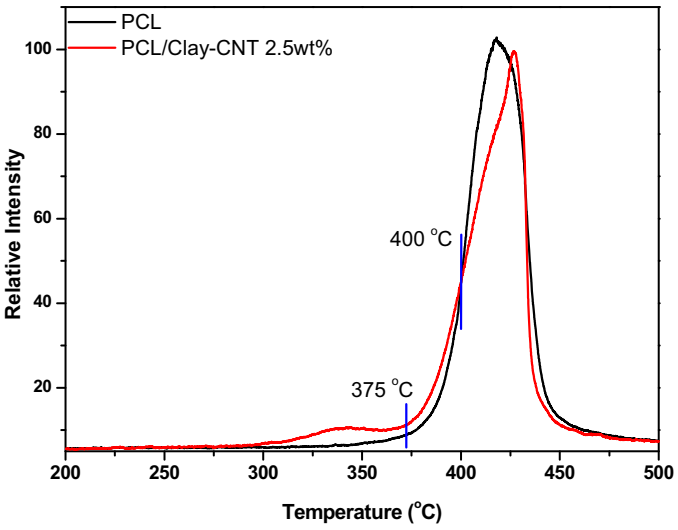

Fig. 14. Evolved Gas Analysis during the pyrolysis of neat PCL and of a PCL/Clay-CNT nanocomposite with a filler content of 2.5 wt%.

stability [47]. The presence of hydroxyls on the surfaces of clays and to a lower extent on the CNTs, can act as Brønsted acidic sites responsible for accelerated degradation rates [48] and this effect seems to overshadow the ability of Clay-CNT to prevent transport of volatile compounds during degradation. Also, the reduced thermal stability is an indication of poor dispersion and lack of covalent bonding between the polymeric matrix and the fillers, as observed with spectroscopic methods.

While TGA is used to study the effect of nanofillers on thermal stability of polymers, pyrolysis-gas chromatography/mass spectroscopy was used to evaluate the mechanism for the thermal degradation of PCL and to determine if and how it is altered by the presence of Clay-CNT. Evolved gas analysis was performed in order to determine the temperature range where gases were produced during the pyrolysis of PCL and PCL/Clay-CNT with 2.5%wt filler. To study the possible effect of the nanofillers on the degradation mechanism of PCL, the temperatures chosen for single-shot analysis were 375 and 400 °C. The results are reported in Fig. 14, where one can see that both samples are stable up to 300 °C, in agreement with the TGA measurements, and decomposition finishes at ~500 °C. In the case of the PCL/Clay-CNT nanocomposite some gases also evolved at temperatures 300–375 °C, indicating that Clay-CNT may catalyse the initiation of PCL decomposition. This is expected due to the presence of clay, even though such a behavior was not observed in the TGA study. The main peak of pyrolysis products appears shifted in the case of the nanocomposite, suggesting delayed release of gases, which could mean that the nanofillers could act as barriers to the diffusion of pyrolysis gases that are released at 425 °C. The recorded chromatographs of the decomposition products during pyrolysis of PCL and PCL/Clay-CNT with 2.5 wt% filler are presented in Fig. 15. The evolved compounds were identified through the collected mass spectra and are presented in Table 4.

Several reports exist concerning the mechanism of thermal degradation of PCL, with varying results. Persenaire et al. distinguished two different degradation steps, the first one consisting in random chain scission with production of 5-hexenoic acid, and the second one comprising only an unzipping depolymerisation and formation of ε-caprolactone monomers [49]. Sivalingam et al. found that under isothermal heating only unzipping reactions occur, while under non-isothermal conditions, both unzipping and *cis*-elimination take place [50]. Aoyagi et al. [51], Abe et al. [52] and Papageorgiou et al. found that random *cis*-elimination

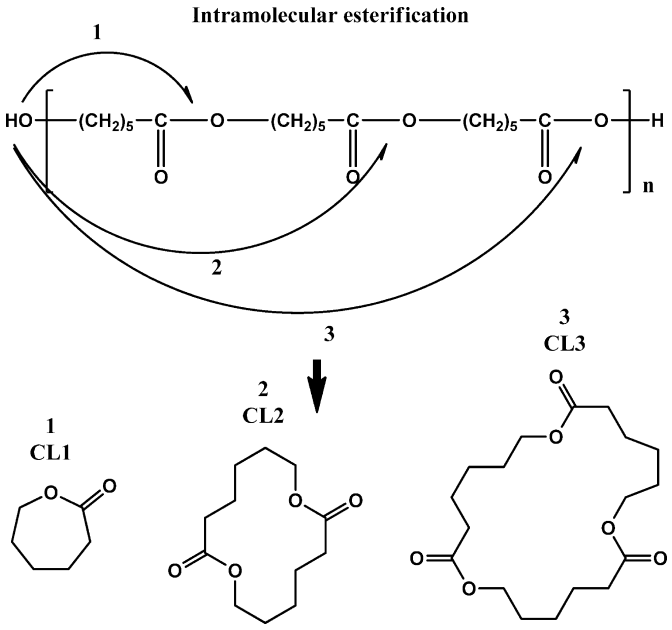

Scheme 1. Intramolecular esterification decomposition mechanism of PCL taking place at low pyrolysis temperatures (370 °C).

and unzipping depolymerization reactions occur simultaneously at high decomposition temperatures, with the first decomposition step being dominated by *cis*-elimination, while in the second step unzipping and/or transesterification reactions compete with random chain scission [53].

The chromatography data of neat PCL pyrolyzed at 370 °C presented in Fig. 15a show 4 main peaks at reaction times, R_t equal to 1.58, 12.03, 23.51 and 34.80 min which mass spectroscopy identifies as CO_2, ε-caprolactone monomer (CL1), its dimer (CL2) and its trimer (CL3). This indicates that degradation occurs via intramolecular transterification. The proposed intramolecular esterification mechanism for the decomposition of PCL that takes place at such low temperatures is presented in Scheme 1 and results in the formation of cyclic monomers and oligomers.

During pyrolysis of PCL at 400 °C, more peaks appear on the chromatograph (Fig. 15a top). Besides ε-caprolactone, its dimer

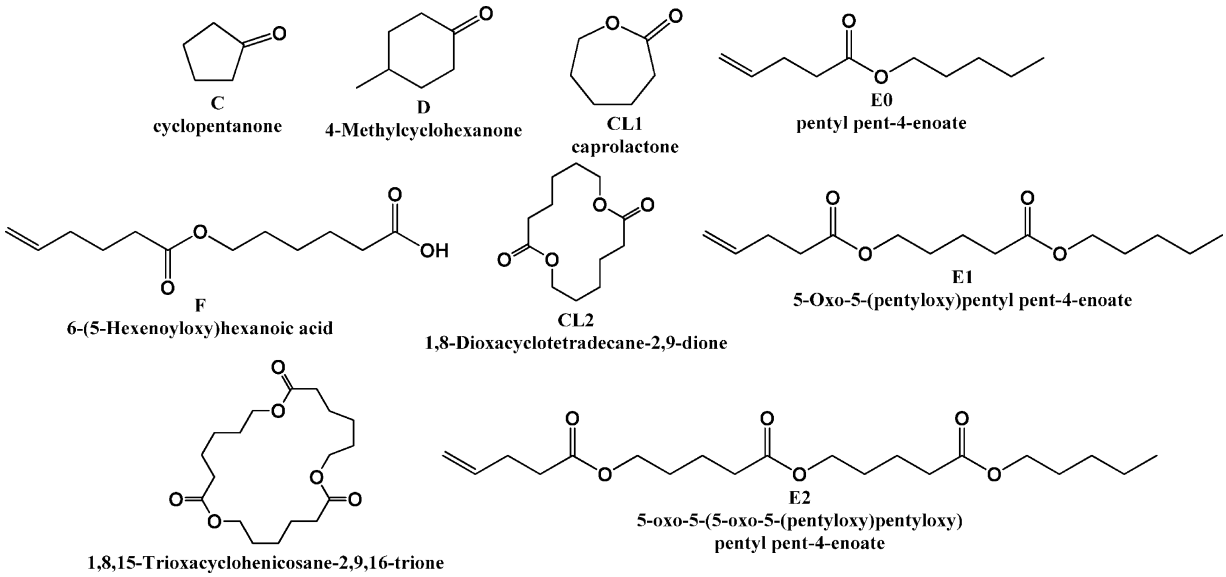

Scheme 2. Identified pyrolysis products of PCL.

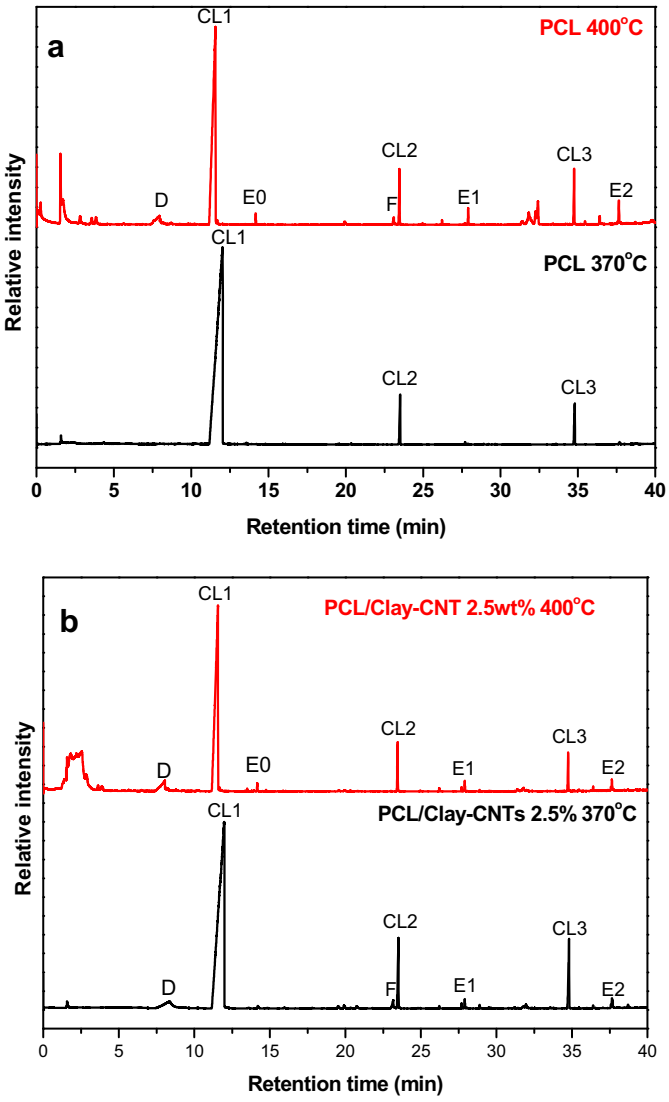

Fig. 15. Pyrolysis-gas chromatography/mass spectroscopy: total ion chromatographs after pyrolysis at 370 and 400 °C of (a) neat PCL and (b) the PCL/Clay-CNT nanocomposite with a filler content of 2.5 wt%.

Table 4
Analysis of evolved gaseous compounds during pyrolysis at 370 and 400 °C of neat PCL and of a PCL/Clay-CNT nanocomposite with 2.5 wt% filler.

Retention Time (min)		Compound		
PCL	PCL/Clay-CNT 2.5 wt%	Peak notation	Assigned compound	Molecular weight
Pyrolysis at 370 °C				
1.58	1.58	–	Carbon dioxide	44
	8.35	D	4-Methylcyclohexanone	114
12.03	11.98	CL1	ε-caprolactone	114
	23.17	F	6-(5-Hexenoyloxy)hexanoic acid	228
23.51	23.52	CL2	1,8-Dioxacyclotetradecane-2,9-dione (epsilon CL dimer)	228
–	27.91	E1	5-Oxo-5-(pentyloxy)pentyl pent-4-enoate	270
34.80	34.81	CL3	1,8,15-Trioxacyclohenicosane-2,9,16-trione (epsilon CL trimer)	342
–	37.70	E2	5-oxo-5-(5-oxo-5-(pentyloxy)pentyloxy) pentyl pent-4-enoate‘	370
Pyrolysis at 400 °C				
1.54	1.57	–	Carbon dioxide	44
	3.90	C	Cyclopentanone	84
7.95	8.05	D	4-Methylcyclohexanone	114
11.57	11.57	CL1	ε-caprolactone	114
14.17	14.17	E0	pentyl pent-4-enoate	170
23.1	–	F	6-(5-Hexenoyloxy)hexanoic acid	228
23.46	23.46	CL2	1,8-Dioxacyclotetradecane-2,9-dione (epsilon CL dimer)	228
27.91	27.90	E1	5-Oxo-5-(pentyloxy)pentyl pent-4-enoate	270
34.76	34.75	CL3	1,8,15-Trioxacyclohenicosane-2,9,16-trione (epsilon CL trimer)	342
37.65	37.65	E2	5-oxo-5-(5-oxo-5-(pentyloxy)pentyloxy) pentyl pent-4-enoate	370

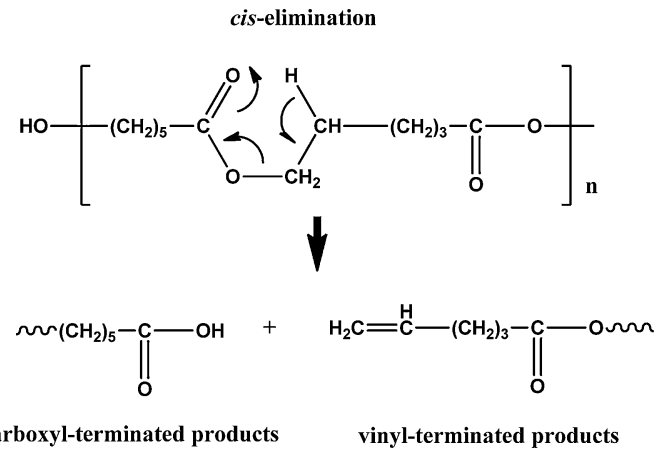

Scheme 3. β-hydrogen bond scission decomposition mechanism of PCL.

and trimer, 5-hexenoic acid (D), 6-(5-Hexenoyloxy)hexanoic acid (F), 5-*O*xo-5-(pentyloxy)pentyl pent-4-enoate (E1) and 5-*O*xo-5-(5-oxo-5-(pentyloxy)pentyloxy)pentyl pent-4-enoate (E2) are identified. Their structures are depicted on Scheme 2. These vinyl- and carboxylic acid terminated products occur after random chain scission via *cis*-elimination at ester bonds (β-hydrogen bond scission), as shown in Scheme 3. Thus, it can be said that the PCL decomposition mechanism is different at 400 °C than that at 370 °C, and degradation takes place with both intramolecular transesterification and *cis*-elimination reactions.

The chromatograph of the PCL/Clay-CNT nanocomposite with 2.5 wt% filler after pyrolysis at 370 °C (Fig. 15b) presents more peaks than neat PCL treated at the same temperature; in fact, all degradation products are detected and not only caprolactone oligomers, indicating that the nanocomposite is less thermally stable than neat PCL and both degradation mechanisms take place already at lower temperature. The Clay-CNT hybrid hence catalyzes the decomposition of PCL. At 400 °C the same degradation products are identified but peaks corresponding to derivatives produced by *cis*-elimination (D, E0, E1, E2) are more intense. One can therefore conclude that as for neat PCL, *cis*-elimination chain scission reactions are favored at higher degradation temperatures. CO_2 is detected in all chromatographs and results from decarboxylation of carboxylic end groups of PCL and other carboxyl-terminated pyrolysis products. Also, the peak that corresponds to ε-caprolactone monomer (CL1) has relative intensity 100% in all chromatographs, identifying the monomer as the main decomposition product.

4. Conclusions

Nanocomposites based on PCL with clay-CNT nanoadditives were successfully prepared with melt mixing. It was found that tensile strength at break enhanced for nanofiller concentration 0.5–1 wt%, while Young's modulus was increased by increasing clay-CNTs content. The fillers were exfoliated in the polymeric matrix, but no covalent interactions were detected based on XPS and FTIR measurements. Under isothermal conditions, the rate of crystallization decreased drastically with increasing the temperature. Crystallization half-times were also decreased for the nanocomposites, which show that isothermal crystallization proceeds faster since filler particles cause heterogeneous nucleation. The presence of hydroxyls on the surfaces of clays and to a lower extent on the CNTs accelerated degradation rates of PCL as found by TG. In all samples degradation occurs mostly via intramolecular transesterification reactions, and/or unzipping reactions from the α-carboxylic acid chain-ends at 370 °C, while at 400 °C *cis*-elimination also takes place, thus this secondary mechanism is favored at higher temperatures. The predominant mechanism remains intramolecular transesterification in all temperatures.

Acknowledgements

This research has been co-financed by European Union – European Social Fund and Greek National Funds through the Operational Program "Education and Lifelong Learning" of the National Strategic Reference Framework (NSRF) – Research Funding Program: THALES – Investing in knowledge society through the European Social Fund (MIS 377278).

References

[1] R.A. Gross, B. Kalra, Biodegradable polymers for the environment, Science 2 (2002) 803–807, http://dx.doi.org/10.1126/science.297.5582.803.
[2] V.J. Mkhabela, S.S. Ray, Poly(ε-caprolactone) nanocomposite scaffolds for tissue engineering: a brief overview, J. Nanosci. Nanotechnol. 14 (2014) 535–545, http://dx.doi.org/10.1166/jnn.2014.9055.
[3] T.K. Dash, V.B. Konkimalla, Poly-ε-caprolactone based formulations for drug delivery and tissue engineering: a review, J. Controll. Rel. 158 (2012) 15–33, http://dx.doi.org/10.1016/j.jconrel.2011.09.064.
[4] J.L. Hedrick, T. Magbitang, E.F. Connor, T. Glauser, W. Volksen, C.J. Hawker, V.Y. Lee, R.D. Miller, Application of complex macromolecular architectures for advanced microelectronic materials, Chem.—Eur. J. 8 (2002) 3308–3319, http://dx.doi.org/10.1002/1521-3765(20020802)8:15<3308:AID-CHEM3308>3.0.CO;2-D.
[5] Y. Ikada, H. Tsuji, Biodegradable polyesters for medical and ecological applications, Rapid. Commun. 21 (2000), http://dx.doi.org/10.1002/(SICI)1521-3927(20000201)21:3<117:AID-MARC117>3.0.CO;2-X.
[6] Q.T. Nguyen, D.G. Baird, Preparation of polymer-clay nanocomposites and their properties, Adv. Polym. Tech. 25 (2006) (2006) 270–285, http://dx.doi.org/10.1002/adv.20079.
[7] G. Pandey, E.T. Thostenson, Carbon nanotube-based multifunctional polymer nanocomposites, Polym. Rev. 52 (2012) 355–416, http://dx.doi.org/10.1080/15583724.2012.703747.
[8] D. Gournis, M.A. Karakassides, T. Bakas, N. Boukos, D. Petridis, Catalytic synthesis of carbon nanotubes on clay minerals, Carbon 40 (2002) 2641–2646, http://dx.doi.org/10.1016/S0008-6223(02)00165-3.
[9] V. Georgakilas, D. Gournis, M.A. Karakassides, A. Bakandritsos, D. Petridis, Organic derivatization of single-walled carbon nanotubes by clays and intercalated derivatives, Carbon 42 (2004) 865–870, http://dx.doi.org/10.1016/j.carbon.2004.01.064.
[10] T. Tsoufis, L. Jankovic, D. Gournis, P.N. Trikalitis, T. Bakas, Evaluation of first-row transition metal oxides supported on clay minerals for catalytic growth of carbon nanostructures, Mater. Sci. Eng. B 152 (2008) 44–49, http://dx.doi.org/10.1016/j.mseb.2008.06.029.
[11] J.T. Yeh, M.-C. Yang, C.-J. Wu, C.S. Wu, Preparation and characterization of biodegradable polycaprolactone/multiwalled carbon nanotubes nanocomposites, J. App. Pol. Sci. 112 (2009) 660–668, http://dx.doi.org/10.1002/app.29485.
[12] G. Xu, L. Du, H. Wang, R. Xia, X. Meng, Q. Zhu, Nonisothermal crystallization kinetics and thermomechanical properties of multiwalled carbon nanotube-reinforced poly((-caprolactone) composites, Polym. Int. 57 (2008) 1052–1066, http://dx.doi.org/10.1002/pi.2448.
[13] K. Litina, A. Miriouni, D. Gournis, M.A. Karakassides, N. Georgiou, E. Klontzas, E. Ntoukas, A. Avgeropoulos, Nanocomposites of polystyrene-b-polyisoprene copolymer with layered silicates and carbon nanotubes, Eur. Polym. J. 42 (2006) 2098–2107, http://dx.doi.org/10.1016/j.eurpolymj.2006.03.025.
[14] A. Enotiadis, K. Litina, D. Gournis, S. Rangou, A. Avgeropoulos, P. Xidas, K. Triantafyllidis, Nanocomposites of polystyrene-b-poly(isoprene)-b-polystyrene triblock copolymer with clay-carbon nanotube hybrid nanoadditives, J. Phys. Chem. B 117 (2013) 907–915, http://dx.doi.org/10.1021/jp309361b.
[15] W.-D. Zhang, I.Y. Phang, T.X. Liu, Growth of carbon nanotubes on clay: unique nanostructured filler for high-performance polymer nanocomposites, Adv. Mater. 18 (2006) 73–77, http://dx.doi.org/10.1002/adma.200501217.
[16] Z. Wang, C. Xu, Y. Zhao, D. Zhao, Z. Wang, H. Li, K.-T. Lau, Fabrication and mechanical properties of exfoliated clay-CNTs/epoxy nanocomposites, Mater. Sci. Eng. A 490 (2008) 481–487, http://dx.doi.org/10.1016/j.msea.2008.01.040.
[17] Y.-Q. Zhao, K.-T. Lau, Z. Wang, Z.-C. Wang, H.-Y. Cheung, Z. Yang, H.-L. Li, Fabrication and properties of clay-supported carbon nanotube/poly (vinyl alcohol) nanocomposites, Polym. Compos. 30 (2009) 702–707, http://dx.doi.org/10.1002/pc.20698.
[18] S. Santangelo, G. Gorrasi, R. Di Lieto, S. De Pasquale, G. Patimo, E. Piperopoulos, M. Lanza, G. Faggio, F. Mauriello, G. Messina, C. Milone, Polylactide and carbon nanotubes/smectite-clay nanocomposites: preparation, characterization, sorptive and electrical properties, Appl. Clay Sci. 53 (2011) 188–194, http://dx.doi.org/10.1016/j.clay.2010.12.013.
[19] G. Gorrasi, C. Milone, E. Piperopoulos, M. Lanza, A. Sorrentino, Hybrid clay mineral-carbon nanotube-PLA nanocomposite films. Preparation and photodegradation effect on their mechanical, thermal and electrical

properties, Appl. Clay Sci. 71 (2013) 49–54, http://dx.doi.org/10.1016/j.clay.2012.11.004.
[20] G. Gorrasi, S. D'Ambrosio, G. Patimo, R. Pantani, Hybrid clay-carbon nanotube/PET composites: preparation, processing, and analysis of physical properties, J. Appl. Polym. Sci. 131 (2014) 40441, http://dx.doi.org/10.1002/APP.40441.
[21] D. Gournis, A. Mantaka-Marketou, M.A. Karakassides, D. Petridis, Ionizing radiation-induced defects in smectite clays, Phys. Chem. Miner. 28 (2001) 285–290, http://dx.doi.org/10.1007/s002690100153.
[22] P. Louette, F. Bodino, J.-J. Pireaux, Poly(methyl methacrylate) (PMMA) XPS reference core level and energy loss spectra, Spectra 12 (2005) 27–31, http://dx.doi.org/10.1116/11.20050914.
[23] J. Watts, High Resolution XPS of Organic Polymers: The Scienta ESCA 300 Database, John Wiley & Sons, Chichester, 1992, http://dx.doi.org/10.1002/sia.740200310, Surf. Interface Anal. 20.
[24] E. Maccallini, T. Tsoufis, A. Policicchio, S. La Rosa, T. Caruso, G. Chiarello, E. Colavita, V. Formoso, D. Gournis, R.G. Agostino, A spectro-microscopic investigation of Fe-Co bimetallic catalysts supported on MgO for the production of thin carbon nanotubes, Carbon 48 (2010) 3434–3445 http://dx.doi.org/10.1016/j.carbon.2010.05.039.
[25] T. Tsoufis, P. Xidas, L. Jankovic, D. Gournis, A. Saranti, T. Bakas, M. Karakassides, Catalytic production of carbon nanotubes over Fe-Ni bimetallic catalysts supported on MgO, Diamond Relat. Mater. 16 (2007) 155–160, http://dx.doi.org/10.1016/j.diamond.2006.04.014.
[26] W. Zhu, D. Miser, W. Chan, M. Hajaligol, Characterization of combustion fullerene soot, C60, and mixed fullerene, Carbon 42 (2004) 1463–1471, http://dx.doi.org/10.1016/j.carbon.2004.01.076.
[27] W.C. Oh, F.J. Zhang, M.L. Chen, Synthesis and characterization of V-C_{60}/TiO_2 photocatalysts designed for degradation of methylene blue, J. Ind. Eng. Chem. 16 (2010) 312–326 http://dx.doi.org/10.1016/j.jiec.2009.09.065.
[28] M.J. Allen, V.C. Tung, R.B. Kaner, Honeycomb carbon: a review of graphene, Chem. Rev. 110 (2010) 132–145, http://dx.doi.org/10.1021/cr900070d.
[29] E. Maccallini, G. Kalantzopoulos, T. Tsoufis, R.G. Agostino, G. Chiarello, V. Formoso, T. Caruso, A. Policicchio, D. Gournis, E. Colavita, Metallic tin-filling effects on carbon nanotubes revealed by atomically resolved spectro-microscopies, J. Nano Res. 3 (2008) 1–6, http://dx.doi.org/10.4028/www.scientific.net/JNanoR.3.1.
[30] M. Sveningsson, R.-E. Morjan, O.A. Nerushev, Y. Sato, J. Bäckström, E.E.B. Campbell, F. Rohmund, Raman spectroscopy and field-emission properties of CVD-grown carbon-nanotube films, Appl. Phys. A: Mater. Sci. Process 71 (2001) 409–418, http://dx.doi.org/10.1007/s003390100923.
[31] M.S. Dresselhaus, G. Dresselhaus, A. Jorio, A.G. Souza Filho, R. Saito, Raman spectroscopy of isolated single wall carbon nanotubes, Carbon 40 (2002) 2043–2061, http://dx.doi.org/10.1016/S0008-6223(02)00066-0.
[32] C.A. Furtado, U.J. Kim, H.R. Gutierrez, Ling Pan, E.C. Dickey, P.C. Eklund, Debundling and dissolution of single-walled carbon nanotubes in amide solvents, J. Am. Chem. Soc. 126 (2004) 6095–6105, http://dx.doi.org/10.1021/ja039588a.
[33] W. Li, H. Zhang, C. Wang, Y. Zhang, L. Xu, K. Zhu, S. Xie, Raman characterization of aligned carbon nanotubes produced by thermal decomposition of hydrocarbon vapor, Appl. Phys. Lett. 70 (1997), http://dx.doi.org/10.1063/1.118993.
[34] S. Arepalli, P. Nikolaev, O. Gorelik, V.G. Hadjiev, H.A. Bradlev, W. Holmes, B. Files, L. Yowell, Protocol for the characterization of single-wall carbon nanotube material quality, Carbon 42 (2004) 1783–1791, http://dx.doi.org/10.1016/j.carbon.2004.03.038.
[35] E. Roumeli, E. Pavlidou, E. Avgeropoulos, G. Vourlias, D. Bikiaris, K. Chrissafis, Factors controlling the enhanced mechanical and thermal properties of nanodiamond-reinforced cross-linked high density polyethylene, J. Phys. Chem. B 118 (2014) 11341–11352, http://dx.doi.org/10.1021/jp504531f.
[36] M.L. Flores-Cedillo, K.N. Alvarado-Estrada, A.J. Pozos-Guillen, J.S. Murquia-Ibarra, M.A. Vidal, J.M. Cervantes, R. Rosales-Ibanez, J.V. Cauich-Rodriques, Multiwall carbon nanotubes/polycaprolactone scaffolds seeded with human dental pulp stem cells for bone tissue regeneration, J. Mater. Sci. Mater. Med. 27 (2016) 27–35, http://dx.doi.org/10.1007/s10856-015-5640-y.
[37] O. Boura, E. Diamanti, S.A. Grammatikos, D. Gournis, A.S. Paipetis, Carbon nanotube growth on high modulus carbon fibres: morphological and interfacial characterization, Surf. Interface Anal. 45 (2013) 1372–1381, http://dx.doi.org/10.1002/sia.5292.
[38] K. Spyrou, G. Potsi, E. Diamanti, X. Ke, E. Serestatidou, I. Verginadis, A. Velalopoulou, A. Evangelou, Y. Deligiannakis, G. Van Tendeloo, D. Gournis, P. Rudolf, Towards novel multifunctional pillared nanostructures: effective intercalation of adamantylamine in graphene oxide and smectite clays, Adv. Func. Mater. 24 (2014) 5841–5850, http://dx.doi.org/10.1002/adfm.201400975.
[39] D. Papageorgiou, L. Tzounis, G. Papageorgiou, D. Bikiaris, K. Chrissafis, β-Nucleated propylene-ethylene random copolymer filled with multi-walled carbon nanotubes: mechanical, thermal and rheological properties, Polymer 55 (2014) 3758–3769.
[40] R. Li, K. Nie, X. Shen, S. Wang, Biodegradable polyester hybrid nanocomposites containing titanium dioxide network and poly(ε-caprolactone): synthesis and characterization, Matter. Lett. 61 (2007) 1368–1371, http://dx.doi.org/10.1016/j.matlet.2006.07.032.
[41] M.L. Di Lorenzo, C. Silvestre, Non-isothermal crystallization of polymers, Prog. Polym. Sci. 24 (1999) 917–950, http://dx.doi.org/10.1016/S0079-6700(99)00019-2.
[42] A. Dobreva, I. Gutzow, Activity of substrates in the catalyzed nucleation of glass-forming melts. I. Theory, J. Non-Cryst. Solids 162 (1993) 1–12, http://dx.doi.org/10.1016/0022-3093(93)90736-H.
[43] A. Dobreva, I. Gutzow, Activity of substrates in the catalyzed nucleation of glass-forming melts. II. Experimental evidence, J. Non-Cryst. Solids 162 (1993) 13–25, http://dx.doi.org/10.1016/0022-3093(93)90737-I.
[44] G. Papageorgiou, Z. Terzopoulou, D. Achilias, D. Bikiaris, M. Kapnisti, D. Gournis, Biodegradable poly(ethylene succinate) nanocomposites. Effect of filler type on thermal behaviour and crystallization kinetics, Polymer 54 (2013) 4604–4616, http://dx.doi.org/10.1016/j.polymer.2013.06.005.
[45] G. Papageorgiou, M. Nerantzaki, I. Grigoriadou, D. Papageorgiou, K. Chrissafis, Isotactic polypropylene/multi-walled carbon nanotube nanocomposites: the effect of modification of MWCNTs on mechanical properties and melt crystallization, Macromo. Chem. Phys. 214 (2013) 2415–2431, http://dx.doi.org/10.1002/macp.201300355.
[46] A. Vassiliou, G. Papageorgiou, D. Achilias, D. Bikiaris, Non-isothermal crystallisation kinetics of in situ prepared poly(e-caprolactone)/surface-treated SiO2 nanocomposites, Macromol. Chem. Phys. 208 (2007) 364–376, http://dx.doi.org/10.1002/macp.200600447.
[47] A.R. McLauchin, N.L. Thomas, Preparation and thermal characterisation of poly(lactic acid) nanocomposites prepared from organoclays based on an amphoteric surfactant, Polym. Degrad. Stabil. 94 (2009) 868–872, http://dx.doi.org/10.1016/j.polymdegradstab.2009.01.012.
[48] X. Xu, Y. Ding, Z. Qian, F. Wang, B. Wen, H. Zhou, S. Zhang, M. Yang, Degradation of poly(ethylene terephthalate)/clay nanocomposites during melt extrusion: effect of clay catalysis and chain extension, Polym. Degrad. Stab. 94 (2009) 13–23, http://dx.doi.org/10.1016/j.polymdegradstab.2008.09.009.
[49] O. Persenaire, M. Alexandre, P. Degee, P. Dubois, Mechanisms and kinetics of thermal degradation of poly(ε-caprolactone), Biomacromolecules 2 (2001) 288–294, http://dx.doi.org/10.1021/bm0056310.
[50] G. Sivalingam, R. Karthik, Giridhar Madras, Kinetics of thermal degradation of poly(ε-caprolactone), J. Anal. Appl. Pyrol. 70 (2003) 631–647, http://dx.doi.org/10.1016/S0165-2370(03)00045-7.
[51] Y. Aoyagi, K. Yamashita, Y. Doi, Thermal degradation of poly[(R)-3-hydroxybutyrate], poly[e-caprolactone], and poly[(S)-lactide], and poly[(S)-lactide], Polym. Degrad. Stab. 76 (2002) 53–59, http://dx.doi.org/10.1016/S0141-3910(01)00265-8.
[52] H. Abe, N. Takahashi, K.J. Kim, M. Mochizuki, Y. Doi, Effects of residual zinc compounds and chain-end structure on thermal degradation of poly((-caprolactone), Biomacromolecules 5 (2004) 1480–1488, http://dx.doi.org/10.1021/bm049945p.
[53] D. Papageorgiou, E. Roumeli, Z. Terzopoulou, V. Tsanaktsis, K. Chrissafis, D. Bikiaris, Polycaprolactone/multi-wall carbon nanotube nanocomposites prepared by in situ ring opening polymerization: decomposition profiling using thermogravimetric analysis and analytical pyrolysis-gas chromatography/mass spectrometry, J. Anal. Appl. Pyrol. 115 (2015) 125–131, http://dx.doi.org/10.1016/j.jaap.2015.07.007.